crystals

MDPI

Article

Machine Learning to Predict Workability and Compressive Strength of Low- and High-Calcium Fly Ash–Based Geopolymers

Andrie Harmaji [1,*], Mira Chandra Kirana [2] and Reza Jafari [1,*]

[1] Department of Applied Sciences, University of Québec in Chicoutimi (UQAC), 555, Boul. de l'Université, Saguenay, QC G7H 2B1, Canada
[2] Department of Computer Engineering, Polytechnique Montréal, Montreal, QC H3T 1J4, Canada
* Correspondence: aharmaji@etu.uqac.ca (A.H.); reza_jafari@uqac.ca (R.J.)

Abstract: The potential substitution of Portland cement–based concrete with low- and high-calcium fly ash–based geopolymers was investigated. However, predicting the workability and compressive strength of geopolymers with the desired physical and mechanical properties is a complicated process because of the variety of chemical compositions found in aluminosilicate sources. Therefore, machine-learning techniques were used to predict the physical and mechanical properties of the geopolymers and eliminate the usual trial-and-error laboratory procedures. The experimental and predicted results of geopolymer properties using the multilayer perceptron regressor, voting regressor, and XGBoost techniques were compared. The XGBoost model outperformed the other models in terms of accuracy for predicting workability and compressive strength, producing the R^2 of 0.96 and 0.89, respectively. Sensitivity analysis determined that the percentage of CaO had the largest effect on geopolymer workability of 27.13%. Fly ash content had the largest effect on compressive strength of 34.44%. Our approach offers a straightforward and dependable strategy for designing and optimizing fly ash–based geopolymers.

Keywords: geopolymer; fly ash; machine learning; workability; compressive strength

check for updates

Citation: Harmaji, A.; Kirana, M.C.; Jafari, R. Machine Learning to Predict Workability and Compressive Strength of Low- and High-Calcium Fly Ash–Based Geopolymers. *Crystals* **2024**, *14*, 830. https://doi.org/10.3390/cryst14100830

Academic Editor: George D. Verros

Received: 8 September 2024
Revised: 21 September 2024
Accepted: 22 September 2024
Published: 24 September 2024

Copyright: © 2024 by the authors. Licensee MDPI, Basel, Switzerland. This article is an open access article distributed under the terms and conditions of the Creative Commons Attribution (CC BY) license (https://creativecommons.org/licenses/by/4.0/).

1. Introduction

Geopolymers have emerged as a sustainable alternative to cement because their production requires lower power consumption and emits fewer greenhouse gases, and these compounds have excellent mechanical and durability properties. Geopolymer systems can reduce CO_2 emissions by 50%–80% and energy demand by 60% compared with ordinary Portland cement [1,2]. They are formed by the alkali activation of silica (Si) and alumina (Al)-rich precursors with an alkaline activator. One of the most common raw materials of geopolymers is fly ash [3], a solid waste by-product of coal-fired power plants, for which electrical power plants look for cost-effective and environmentally friendly disposal methods. The chemical composition of fly ash depends on the type of coal, which can be divided into four basic types: anthracite, bituminous, subbituminous, and lignite. Bituminous coal fly ash consists primarily of silica, alumina, iron oxide, and calcium, with varying proportions of carbon [4]. Lignite and subbituminous coal fly ash have higher calcium oxide concentrations, lower percentages of silica and iron oxide, and a lower carbon content [5]. According to ASTM C618 [6], low- and high-calcium fly ash is categorized as Class F and Class C, respectively. Low-calcium Class F fly ash contains less than 10% CaO, whereas high-calcium Class C fly ash contains more than 15% CaO. This higher CaO content produces self-cementing qualities [7], with the geopolymer gradually hardening and becoming stronger over time in the presence of water.

The complexity of the chemical composition makes fly ash–based geopolymers an interesting research topic. However, given the nature and diversity of available source materials, designing a geopolymer mixture that achieves the desired fresh properties, satisfactory

strength characteristics, and proclaimed environmental benefits is a complex process. Its design necessitates a meticulous selection of input material and mix proportions, generally determined through experiments that require a significant amount of material, time, and labor. Thus, it is critical to use soft computing techniques [8] and machine-learning models [9] to quickly and accurately predict the working properties of geopolymers. Machine learning operates on a similar concept to traditional algorithms; they are more favorable for managing nonlinear behavior than linear behavior [10]. Recent research applying machine learning to geopolymers includes Amin et al. [11], who used decision trees (DT) and a support vector machine (SVM) ensemble learner to predict the mechanical properties of fly ash/slag–based geopolymer concrete. Their DT ensemble learner produced an R^2 value of 0.93, a value that was better than in the other tested methods. Huang et al. [12] used gene expression programming (GEP) and multi-expression programming (MEP) to predict the compressive and split tensile strength of fly ash–based geopolymer. The GEP-based models outperformed the MEP-based models for both compressive and split tensile strengths. Most similar studies use machine learning to predict the compressive strength of a geopolymer, but as far as the authors know, there has been no research on predicting a geopolymer's workability.

The purpose of this research is to apply individual and ensemble machine-learning methods using the multilayer perceptron regressor, voting regressor, and XGBoost techniques to predict the workability and compressive strength of geopolymers made using low- and high-calcium fly ash. Then, sensitivity analysis was performed to determine the impact of input parameters on the outcome. The results can then be used to design sustainable geopolymers with the desired performance.

2. Materials and Methods

2.1. Materials

For this study, low- and high-calcium fly ash produced by power stations in Suralaya (fly ash F) and West Sumbawa (fly ash C) in Indonesia, respectively, were used. Particle size analysis (PSA) of the materials was performed using the Fritsch particle sizer (Figure 1), and the chemical composition of both fly ashes was determined using X-ray fluorescence (XRF) (Table 1).

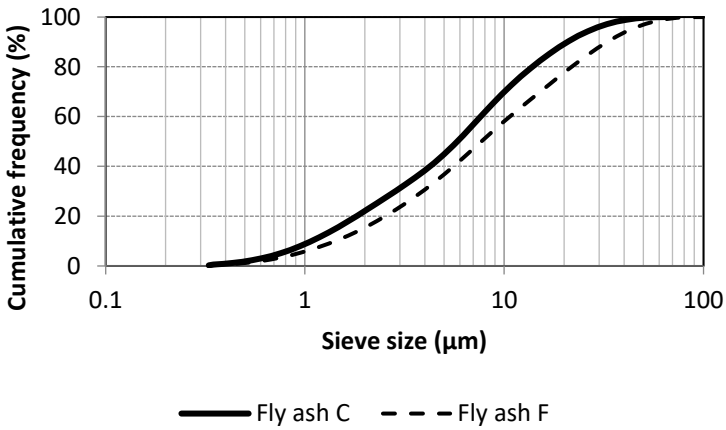

Figure 1. Distribution of particles for low-calcium (Class F) and high-calcium (Class C) fly ash.

X-ray diffraction (XRD) coupled with the XPowder Ver. 2004.04.70 Pro software served to determine the mineral compositions of fly ash. Both fly ashes contained quartz and mullite, and thaumasite appeared in the Class C fly ash (Figure 2). SEM was used to identify the form of the fly ash particles (Figure 3). The Class F fly ash was mostly spherical and contained larger particles than the Class C fly ash. Some of the latter particles had imperfect spherical shapes.

Table 1. The chemical compositions of low- (F) and high-calcium (C) fly ash measured by XRF.

Oxides	Fly Ash F	Fly Ash C
SiO_2	52.30	40.18
Al_2O_3	26.57	17.32
Fe_2O_3	7.28	14.11
CaO	6.00	15.85
Na_2O	1.41	0.93
SO_3	0.70	0.80
K_2O	0.73	1.48
MgO	2.13	6.89
LOI	1.18	0.86

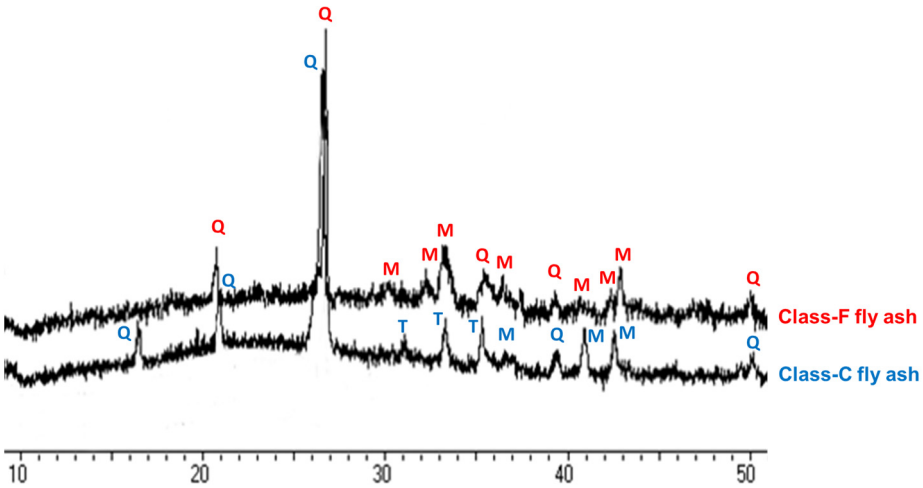

Figure 2. Diffractogram of low- (Class F) and high-calcium (Class C) fly ash. Note: Q, quartz; M, mullite; T, thaumasite.

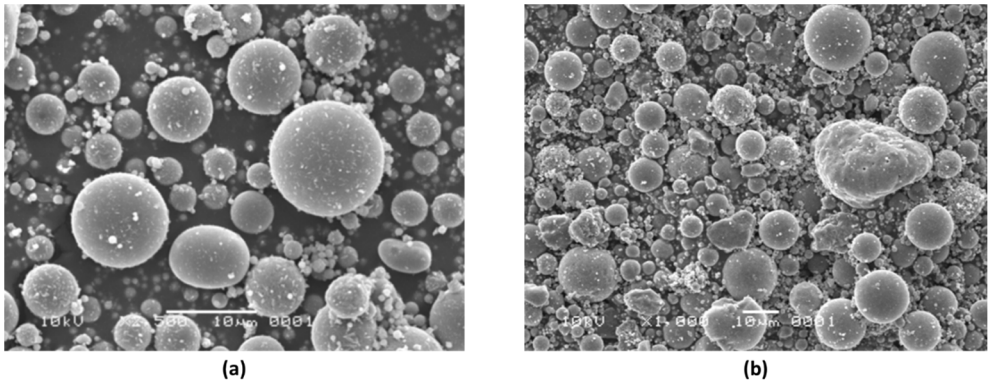

Figure 3. SEM images of (**a**) Class F and (**b**) Class C fly ash.

Sodium hydroxide (NaOH) crystals (98% purity) and a sodium silicate (Na_2SiO_3) solution (15.98% Na_2O, 37.23% SiO_2, and 46.79% H_2O) were obtained from the chemical company Bratachem in Bandung, Indonesia. NaOH working solution was prepared by dissolving NaOH crystals in distilled water. It was then combined with Na_2SiO_3, thoroughly stirred, and left to cool down for six hours before being mixed with the fly ash [13]. Natural sand, as fine aggregate in the saturated-surface-dry (SSD) condition, was supplied from a quarry in Cimalaka, Indonesia, for the production of the geopolymer mortar having an absorption coefficient and fineness modulus of 2.88% and 2.75, respectively.

2.2. Mix Design

The mix proportions for the prepared geopolymers are presented in **Appendix A**, with variations in the amounts of fine aggregate (sand), fly ash, NaOH, Na_2SiO_3, and added water, as well as various CaO, Na_2O, and SiO_2 contents, NaOH molarities, curing temperatures, workabilities, and compressive strengths. These geopolymers were selected for testing because the ratios of fly ash and aggregate and NaOH to Na_2SiO_3, as well as curing temperature, were believed to affect the mechanical properties of geopolymers. Geopolymer slurry was made by combining fly ash, alkali activator, and fine aggregate. Afterward, it was poured into a 50 mm × 50 mm × 50 mm cubical mold.

2.3. Test Methods

2.3.1. Workability Test

A flow test table measurement was conducted in accordance with ASTM C-1437 [14]. This test aims to determine the workability of the sample based on the difference in diameter of the fresh geopolymer. The slurry diameter was measured, then the flow test table was tapped 25 times, and the diameter was remeasured after this tapping.

2.3.2. Compressive Strength Test

The compressive strength testing process followed ASTM C-39 [15] on geopolymer samples aged 7 and 28 days. The testing was conducted using a universal testing machine type RAT 100, which has a load capacity of up to 100 tons. Three specimens were produced for each test, and the presented results were averages of the three.

2.3.3. Characterization Techniques

The chemical composition of the raw material was determined using XRF ADVANT XP Thermo ARL9900 Fourier transform infrared spectroscopy (FTIR), run at 4000 to 400 cm^{-1} at a resolution of 2 cm^{-1} with an average of 32 scans. Measurements were made using a Prestige 21 Shimadzu FTIR spectrometer. Morphological observations were carried out using a Hitachi scanning electron microscope (SEM) SU3500 on a cross section of specimens. X-ray diffraction served to determine the crystallinity and mineral phase of both the raw material and geopolymer. XRD testing was conducted using a Philips Diffractometry PW 1710 XRD instrument. These materials characterization was conducted in Institut Teknologi Bandung, Indonesia.

3. Machine-Learning Algorithms

This research relied on two types of machine-learning models—individual (MLP) and ensemble (VR and XGB)—to evaluate and recommend the most effective model for predicting the desired outcome. Of the 156 data points, 108 were used as training data, and the remaining 48 served as testing data.

3.1. Multilayer Perceptron Regressor (MLP)

Multilayer perceptron (MLP) networks are feedforward neural networks. Multiple layers of a perceptron are arranged in networks called multilayer perceptrons with threshold activation. Vanilla neural networks consist of several perceptrons connected to a single hidden layer. There are three node levels in an MLP: input, hidden, and output. All nodes have a nonlinear activation function and are neurons with the exception of the input nodes. One MLP-supervised learning technique is backpropagation. MLPs are more multilayered than linear perceptrons and have nonlinear activation.

3.2. Voting Regressor (VR)

A voting ensemble is a machine-learning ensemble methodology that boosts system performance by using multiple methods rather than a single model. By combining the outcomes of several techniques, this method can solve problems through classification and regression. The estimators of all models are averaged to obtain a final estimate for regression

problems, for which the ensembles are known as voting regressors (VRs) [16]. Voting can be performed by two means: weighted voting (WV) and average voting (AV). The weights in the case of AV are equal to one. One drawback of AV is that it assumes that each model in the ensemble is equally effective [17]. This assumption is improbable, especially when using different machine-learning algorithms. WV assigns a weight coefficient to every member of the ensemble. The weight can be either a floating-point number between 0 and 1, such that the total equals 1, or an integer representing the number of votes granted to the corresponding ensemble member, starting at 1. Alternatively, it can be an integer representing the number of votes granted to the corresponding ensemble member, starting at 1.

3.3. Extreme Gradient Boosting (XGB)

XGBoost is an ensemble-learning technique based on trees that makes use of the boosting concept [18] and has been widely used because of its great accuracy in a variety of fields [19]. This effective method, which is based on the gradient boosting algorithm (GDB), combines weak models with additional training methods to increase prediction accuracy. Gradient boosting expands the capabilities of the boosting algorithm by combining multiple predictors from a set of weak learners, such as classification and regression trees (CART), to create a new and powerful learner [20]. XGBoost is designed with a multiprocessing OpenMP API, which can use all CPU cores in parallel during training, making it computationally efficient and scalable [21]. Furthermore, XGBoost sorts the independent variables at the start of the training process to reduce training complexity and computational time.

4. Data Processing

4.1. Database Description

The database for the various geopolymer mixtures was obtained from experimental work (presented in **Appendix A**), which involved 156 workability and compressive strength results. The retrieved data were arranged in accordance with the Python coding requirements for each model. The properties of the geopolymers were determined by a variety of factors, including heterogeneity between test methods, mix proportions, preparation methods, and curing conditions. In this study, fly ash amount, CaO content, Na_2O content, SiO_2 content, fine aggregate (sand) amount, NaOH molarity, NaOH amount, Na_2SiO_3 amount, added water amount, and curing temperature were used as input parameters to assess the effect on the 28-day compressive strength. The attributes of fly ash, fine aggregate, NaOH, Na_2SiO_3, and added water are expressed in grams, whereas the oxides (CaO, Na_2O, and SiO_2) are displayed as a percentage (%). Finally, the curing temperature is denoted in degrees Celsius (°C). The summary of input variables and descriptive statistics, including mean, median, mode, standard deviation, input ranges, and lower and upper limits, are presented in Table 2.

Table 2. Descriptive statistics of the input variables.

Variable Parameter	Fly Ash (g)	CaO (%)	Na_2O (%)	SiO_2 (%)	Fine Aggregate (g)	NaOH Molarity	NaOH (g)	Na_2SiO_3 (g)	Added Water (g)	Curing Temp. (°C)
Mean	880.38	9.98	1.22	47.41	1321.25	11.62	183.30	257.56	24.59	75.78
Median	630	6.00	1.41	52.30	1134	12	157.5	210	0	80
Mode	1260	6.00	1.41	52.30	1890	12	315	315	0	80
Standard deviation	367.71	4.88	0.24	6.00	570.53	3.19	87.68	112.23	35.18	14.75
Input range	300	9.85	0.48	12.12	1768	8	258.33	306.67	113.4	60
Lower limit	330	6.00	0.93	40.18	500	8	56.67	113.33	0	20
Upper limit	630	15.85	1.41	52.30	2268	16	315	420	113.4	80

The MLP, VR, and XGB algorithms were used to predict the required output. The predicted compressive strength (C-S) result was then calculated as an R^2 value. A higher R^2 value indicates that the selected model produces better results with a higher precision [22,23].

4.2. Evaluation Criteria

The performance of the resulting model was compared with existing models using the statistical metrics of the correlation coefficient (R^2), mean absolute error (MAE), and mean square error (MSE). Statistical analysis served to evaluate the predictive ability of models in co-occurrence with Equations (1)–(3):

$$R^2 = 1 - \frac{\sum_{k=1}^{n}\left(Y_i - \hat{Y}_i\right)^2}{\sum_{k=1}^{n}\left(Y_i - \mu\right)^2}, \tag{1}$$

$$MAE = \frac{\sum_{i=1}^{n}\left|Y_i - \hat{Y}_i\right|}{n}, \ and \tag{2}$$

$$MSE = \frac{1}{n}\sum_{i=1}^{n}\left(Y_i - \hat{Y}_i\right)^2, \tag{3}$$

where Yi is the observed values, $\hat{Y}i$ is the predicted values, n is the number of data points, and μ is the total number of data points.

5. Results and Discussion

This section covers the analysis of workability tests from the flow test table, compressive strength, chemical and morphological characterization, and machine learning–related prediction. Generally, a water-per-cement (w/c) ratio is used in Portland cement–based concrete systems to correlate w/c with workability and compressive strength. However, because of the complexity of the geopolymer raw material, adjustments were required. The w/c was modified to the mole's ratio of $H_2O/[Na_2O + Al_2O_3 + SiO_2]$ or H/NSA, as recommended by an earlier study [24]. The moles of H_2O were the sum of mol H_2O in Na_2SiO_3, NaOH flakes, NaOH solution, and added water. Additionally, the moles of Na_2O were the sum of Na_2O moles in fly ash, Na_2SiO_3, and NaOH flakes. Furthermore, the moles of SiO_2 were the sum of mol Na_2O in fly ash and Na_2SiO_3. Finally, the moles of Al_2O_3 were obtained from the mol of Al_2O_3 in fly ash.

5.1. Workability Test

The workability of the geopolymer with different H/NSA ratio connections is displayed in Figure 4. Usually, adding more water to the geopolymer-based system will increase the workability of the fresh concrete [25]. This was not the case for the geopolymer mixtures in this study as low H/NSA (range 1–1.5) in the low-calcium fly ash–based geopolymers had high workability, even at a H/NSA less than 2.

Several factors can affect the workability of geopolymers [26], e.g., the high CaO content in the high-calcium fly ash can alter the workability of geopolymer slurries. Adding extra water, therefore, triggers a dual reaction: (i) geopolymerization with the product of sodium aluminum silicate hydrate (NASH) and (ii) hydration that results in calcium silicate hydrate (CSH). These reactions explain why the workability of the high-calcium fly ash was generally low, even at H/NSA values > 2. Thus, working with high-calcium fly ash–based geopolymers is more difficult as they possess low workability and are more difficult to cast into a mold. Moreover, there is a possibility of segregation that must be considered. Flash setting can also occur because of the high calcium content of fly ash [27]. A previous study [28] reported the effectiveness of borax in deterring flash setting time as a means of prolonging the setting time. The particle size of fly ash can also affect the workability of fresh geopolymers. Visually, the particle size of the Class C fly ash was relatively finer than that of the Class F fly ash (Figure 3). Thus, the solubility of fly ash increased as particle size decreased because finer particles can react with alkali activators quickly and produce the aforementioned phenomenon of dual reaction.

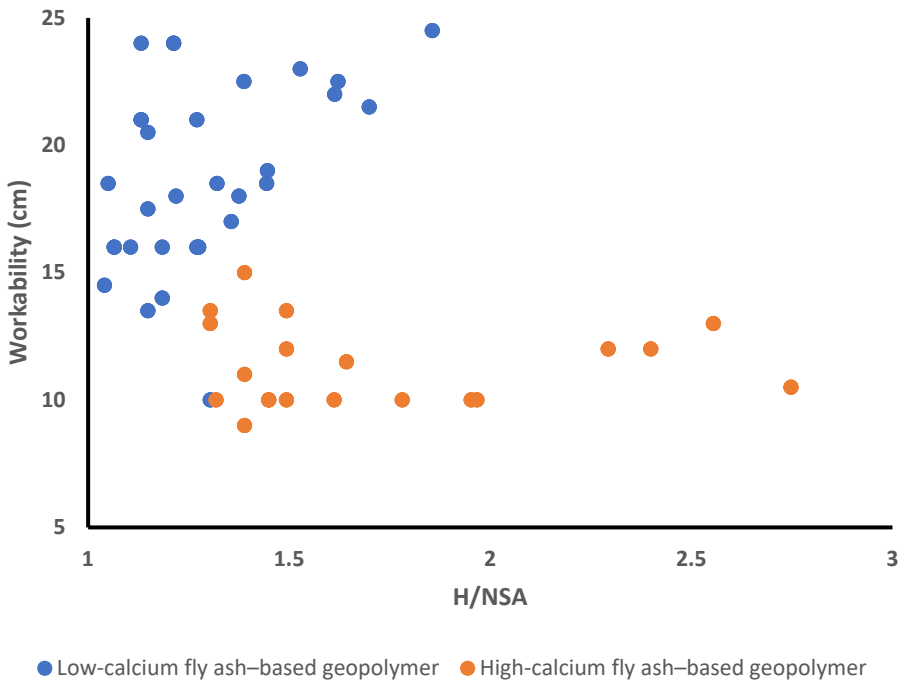

Figure 4. Workability of the geopolymers differing in H/NSA ratios.

5.2. Compressive Strength

Figure 5 displays the relationship between geopolymer compressive strength and H/NSA ratio. The strength difference mentioned above can be explained by the reaction that occurred in low- and high-calcium fly ash–based geopolymers.

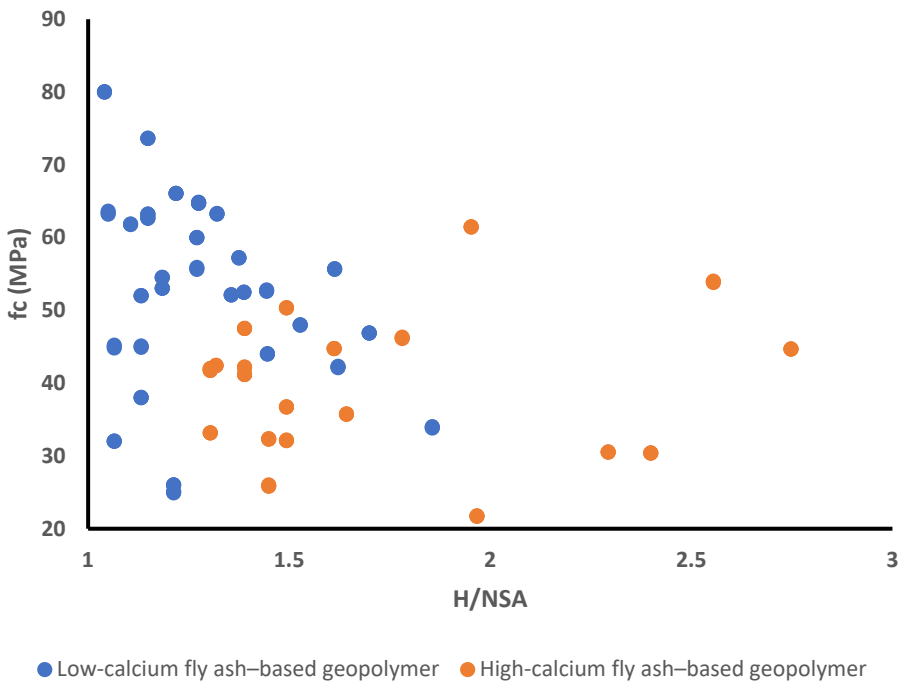

Figure 5. The compressive strength (fc) of geopolymers varying in water/cement (H/NSA) ratio after 24 h of oven curing followed by ambient curing until day 28.

Typically, the primary reaction product in geopolymers is NASH [28], which was the case for our low-calcium fly ash–based geopolymer. This compound has a gel-like form that enhances the mechanical properties and durability of the geopolymer [29]. However, the presence of high calcium in the fly ash favors the possibility of carbonation, which may

result from the alkaline geopolymer mixture coming into contact with atmospheric CO_2 [30]. The process of carbonation in alkali-activated geopolymers is evidently dissimilar from Portland cement–based cementitious material [31]. The pore solution in Portland cement paste dissolves atmospheric CO_2, which then quickly reacts with portlandite to form $CaCO_3$ and with CSH to form both $CaCO_3$ and silica gel [32]. Conversely, because of the absence of portlandite in the geopolymer compound, the natural carbonation takes place directly to form a calcium aluminosilicate hydrate gel (CASH), producing a strong decalcification and residual siliceous gel that also contains alumina in addition to $CaCO_3$ [33].

5.3. Characterization Techniques

The XRD, FTIR, and SEM analyses were conducted on geopolymers with the highest compressive strength and low-calcium (79.96 MPa) and high-calcium (61.45 MPa) fly ash. The following subsections present the diffractograms, spectra, and morphological behaviors of the tested geopolymers.

5.3.1. XRD Analysis

Figures 6 and 7 present the respective diffractograms of Class F fly ash, Class C fly ash, and their associated geopolymerization products. The chemical compositions were analyzed using XPowder Ver. 2004.04.70 Pro software.

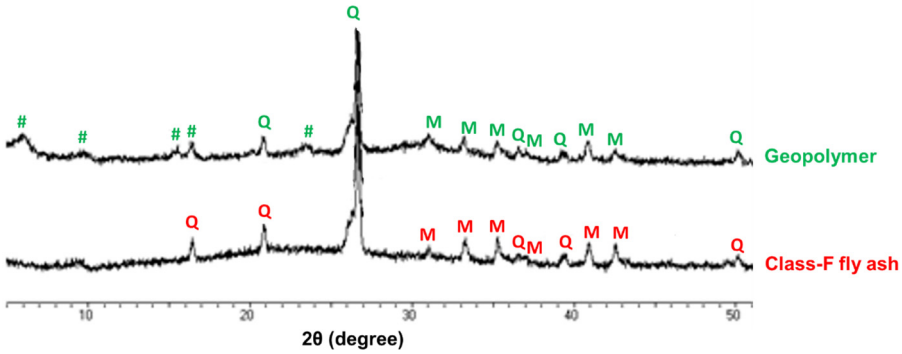

Figure 6. The diffractogram of the low-calcium Class F fly ash and its associated geopolymer.

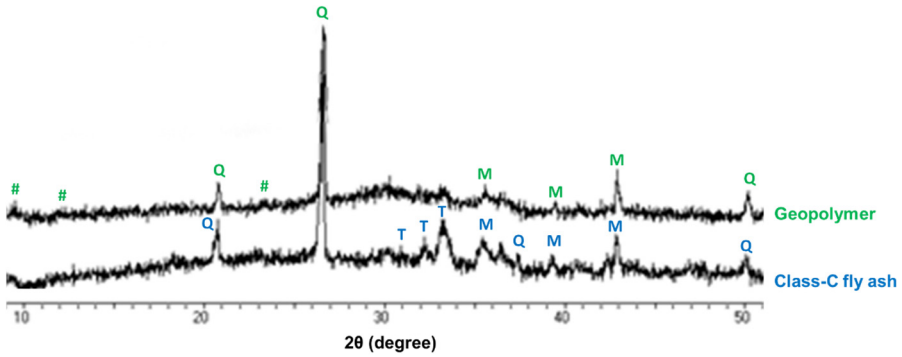

Figure 7. The diffractogram of high-calcium Class C fly ash and its associated geopolymer.

Both fly ashes show the presence of quartz (Q) and mullite (M). These compounds were also reported by Kozhukhova et al. [34]. The calcium-based mineral thaumasite (T) was also present in the Class C fly ash. This result confirmed the high calcium content of the material. However, peak intensity transformed from crystalline to semi-crystalline to amorphous in the geopolymer. The product of both fly ashes contained a sodium silicate hydrate (#) mineral, which confirmed that geopolymerization had occurred.

5.3.2. FTIR Analysis

FTIR served to determine the chemical composition of the geopolymers having the highest strengths of the low- and high-calcium fly ash. The respective spectra are presented in Figures 8 and 9, and the data are summarized in Table 3.

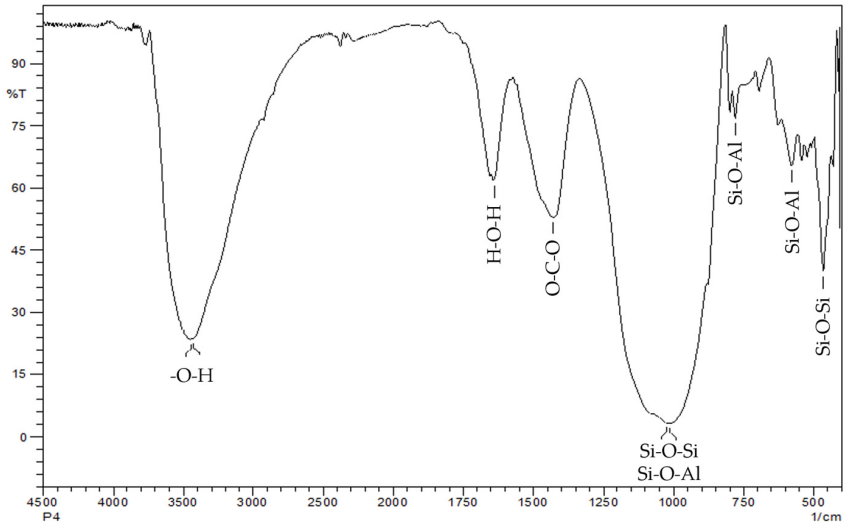

Figure 8. FTIR spectra of the strongest Class C fly ash–based geopolymer.

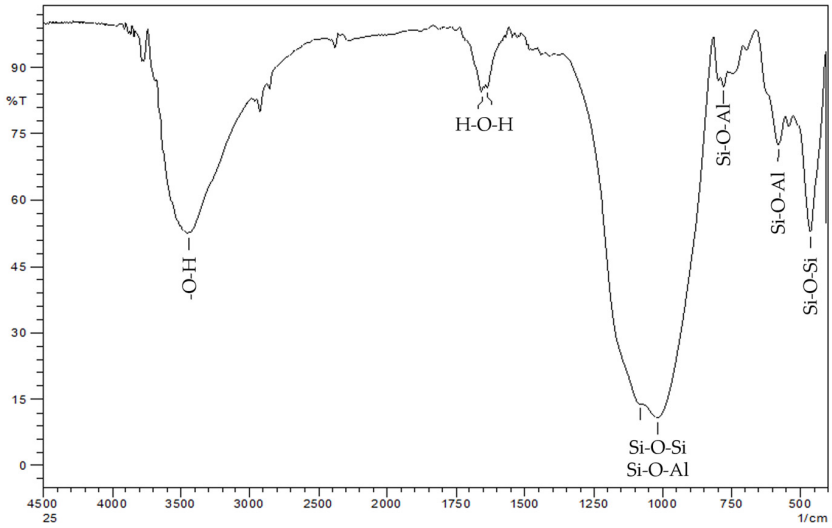

Figure 9. FTIR spectra of the strongest Class F fly ash–based geopolymer.

Table 3. Summary of the FTIR spectra of the geopolymers.

Raw Material	Bending Si–O–Si O–Si–O (cm^{-1})	Vibration Si–O–Al (cm^{-1})	Stretching Si–O–Si Si–O–Al (cm^{-1})	Stretching O–C–O (cm^{-1})	Bending H–O–H (cm^{-1})	Stretching –OH (cm^{-1})
Class C fly ash	464.84	578.64 777.31	1010.70 1024.20	1429.50	1641.42	3448.72
Class F fly ash	462.92	578.64 777.31	1018.41 1080.14	–	1637.56	3448.72

Several similar chemical compositions were found in both samples. The stretching OH and bending H–O–H vibrations of the bound water molecules were detected at around 3448 and 1640 cm^{-1}, respectively [35,36]. A prominent peak at 1024–1200 cm^{-1} can be

observed, which is ascribed to the stretching vibration of the aluminosilicate Si–O–Si and Al–O–Si groups [37]. This absorption band also indicates the presence of a geopolymer compound mineral [38]. The bands around 578–700 cm^{-1} are generated by a Si–O–Al stretching vibration [39,40]. A Si–O–Si bending vibration at around 450 cm^{-1} is also observed [41]. The only notable difference between the two spectra is the presence of an asymmetric stretching O–C–O bond at 1429 cm^{-1} [42] in the geopolymer with high-calcium fly ash. These spectra indicate the existence of sodium carbonate produced through the interaction of excessive sodium and ambient CO_2 [43]. The primary phases that could be formed were anhydrous sodium carbonates (Na_2CO_3), natron ($Na_2CO_3 \cdot 10H_2O$), nahcolite ($NaHCO_3$), trona ($Na_3H(CO_3)_2 \cdot 2H_2O$), and thermonatrite ($Na_2CO_3 \cdot H_2O$) [44]. Alkalis from the activators react with CO_2 to form these compounds, and CO_2 may also interact with the aluminosilicate gel's structure [45]. The alkali activator used in the geopolymer formulation determines how much alkali is available to react with CO_2. Additional soluble silicate from the activator lowers the concentration of free alkalis [46]. This generates carbonation at a slower rate than at which NaOH is formed, which may affect pore structure [47]. Therefore, further investigation and empirical confirmation are necessary to determine the long-term stability of these geopolymers, particularly in regard to their resistance to carbonation [48].

5.3.3. SEM Analysis

The morphology of geopolymer products with low- and high-calcium fly ash is represented in Figures 10 and 11, respectively. The images show the interfacial transition zone (ITZ), which is a zone around the aggregate [49]. The ITZs experience microcrack formation as a result of the strength variations between the ITZs and the paste and aggregate [50]. The geopolymer with high-calcium fly ash displayed a wider crack distance than the low-calcium fly ash–based geopolymer. Nevertheless, a previous study reported that the geopolymer ITZ has more favorable mechanical properties and a stronger bond than Portland cement–based cementitious material [51].

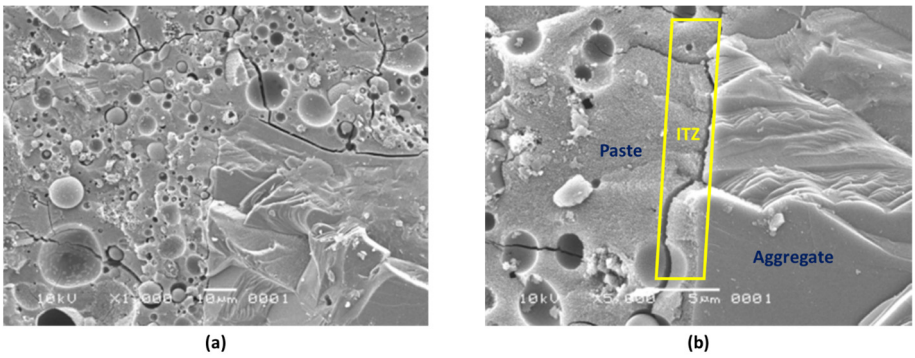

Figure 10. SEM images of the high-calcium Class C fly ash–based geopolymer having the highest strength at (**a**) 1000× (**b**) 5000× magnification.

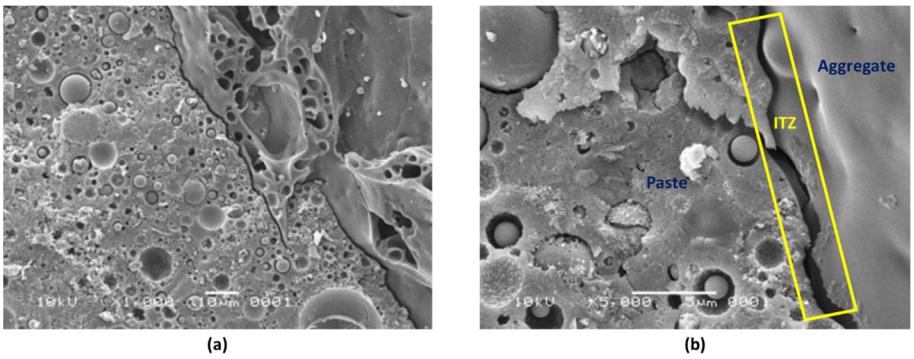

Figure 11. SEM images of the low-calcium Class F fly ash–based geopolymer having the highest strength at (**a**) 1000× (**b**) 5000× magnification.

5.4. Performance Evaluation of Various Models

5.4.1. Workability Prediction

Figure 12 presents the correlation between the actual workability results and the MLP, VR, and XGB models' predictions. Of these three models, the XGB model produced a greater accuracy.

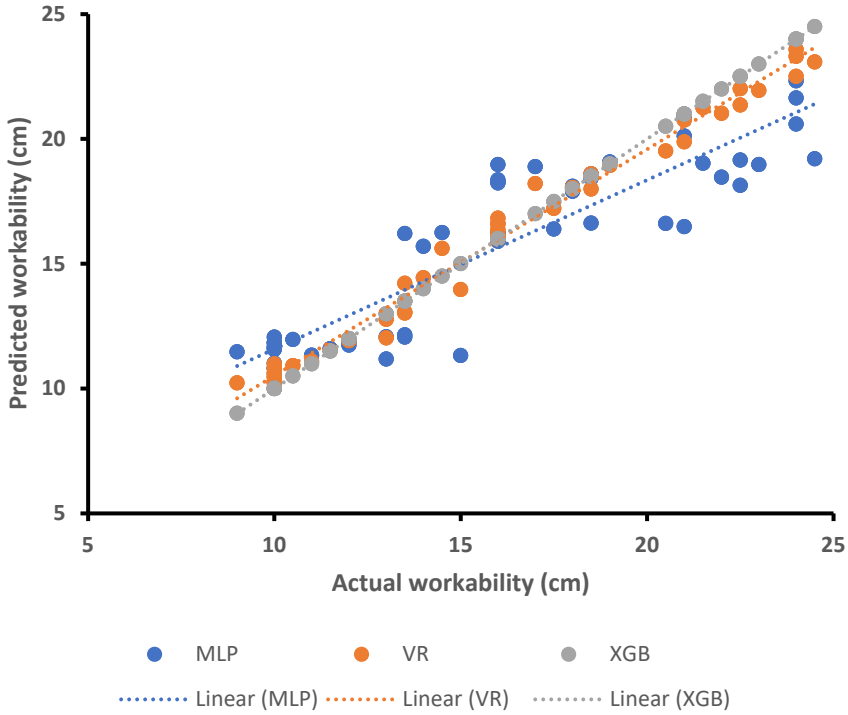

Figure 12. Actual and predicted workability distribution determined by the multilayer perceptron (MLP), voting regressors (VRs), and extreme gradient boosting (XGB) models.

Table 4 presents the statistical measures of predictions for the geopolymer compressive strength from the various machine-learning methods. The MAE, MSE, and R^2 values of the MLP model were higher than those of the MLP and VR models. These values confirm the high accuracy of the XGB model in predicting geopolymer workability.

Table 4. Statistics for the workability predictions of the machine-learning models.

Machine-Learning Methods	MAE (cm)	MSE (cm)	R^2
MLP	1.87	4.81	0.78
VR	1.31	2.39	0.89
XGB	0.06	0.007	0.96

5.4.2. Compressive Strength Prediction

The correlation coefficients for the actual compressive strength versus the predictions made by the MLP, VR, and XGB models (Figure 13) show that the results from the MLP and VR are less accurate than those from the XGB model.

Table 5 presents the statistical measures for the geopolymer compressive strength prediction from different machine-learning methods. The MAE, MSE, and R^2 values for the MLP model have a higher value than the MLP and VR models. Similar to workability prediction, the results illustrated the reliability of the XGB model in forecasting geopolymer strength.

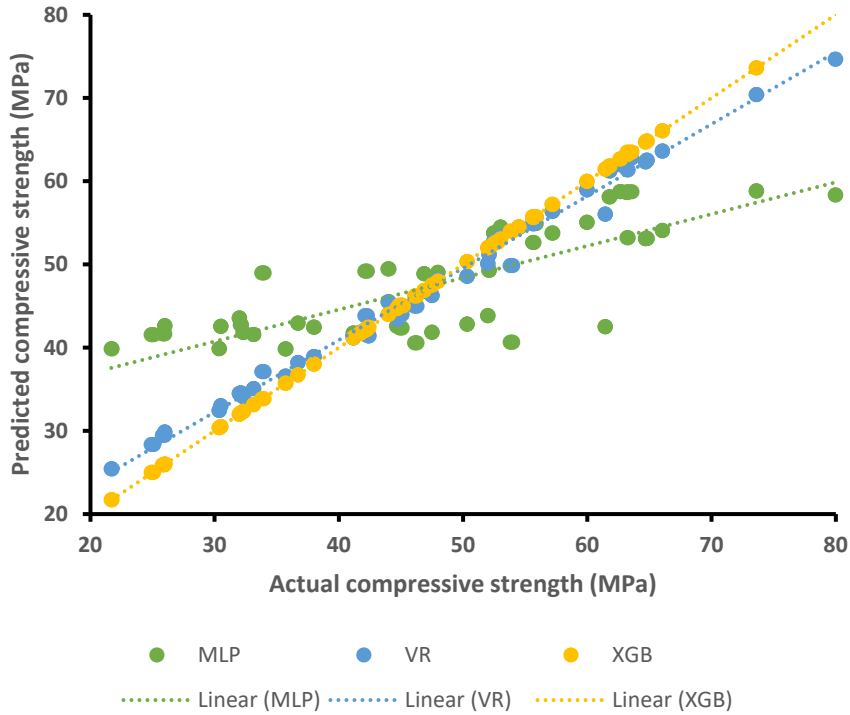

Figure 13. Actual and predicted compressive strength distributions determined by the multilayer perceptron (MLP), voting regressors (VRs), and extreme gradient boosting (XGB) models.

Table 5. Statistics for compressive strength prediction by machine learning.

Machine-Learning Methods	MAE (MPa)	MSE (MPa)	R^2
MLP	7.20	87.37	0.54
VR	5.23	47.43	0.75
XGB	2.45	19.57	0.89

5.5. Feature Importance

The input parameters that affect geopolymer workability and compressive strength predictions were determined. The desired outcome can be significantly affected by the number of input parameters [52,53]. Our approach reduces network complexity by making it easier to identify the most important input parameters and ignore the less important ones [54]. The sensitivity of the XGB-based prediction model was evaluated to look into the contribution of different independent parameters to compressive strength. Equations (4) and (5) were used to compute the variables' participation in the models' outcomes.

$$N_i = f_{max}(x_i) - f_{min}(x_i), and \tag{4}$$

$$S_i = \frac{N_i}{\sum_{j-1}^{n} N_j}. \tag{5}$$

Figures 14 and 15 illustrate how each parameter affects the workability and compressive strength, respectively. Results from feature importance analysis are proportionate to the input variables and total data set used in the model's construction. Nevertheless, the machine-learning algorithm recognizes the impact of each configuration.

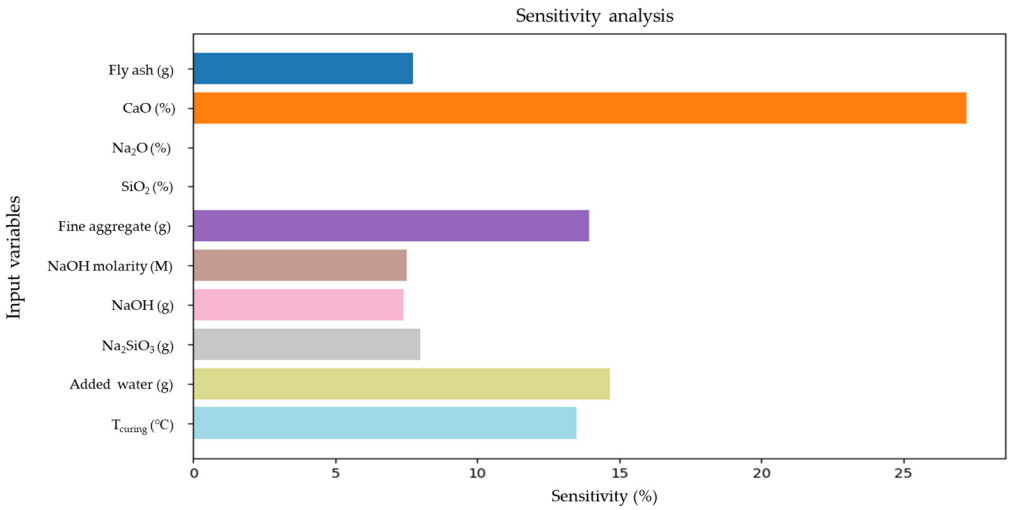

Figure 14. Percentage contribution of the input variable to predicted workability.

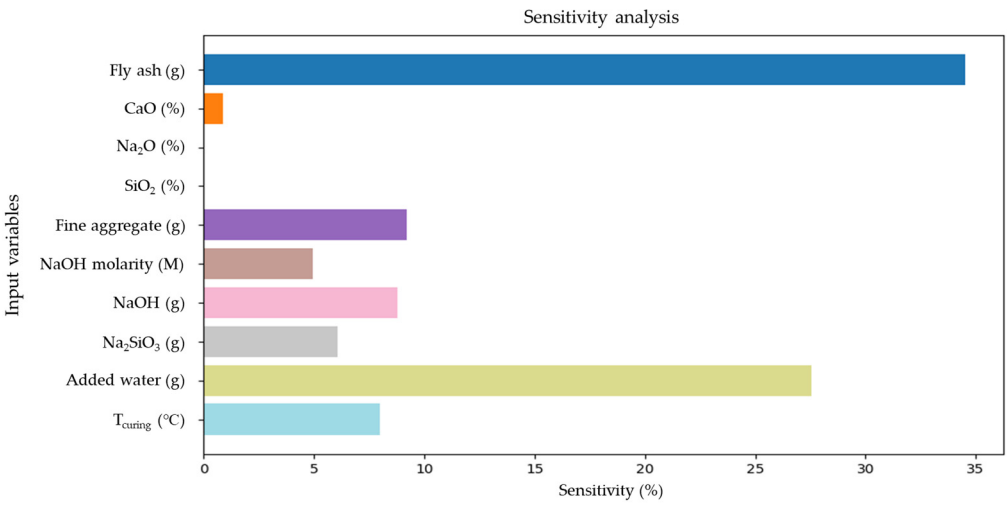

Figure 15. Percentage contribution of the input variables to predicted compressive strength.

The results of the XGB sensitivity testing indicated that CaO percentage (27.13%), added water (14.59%), and fine aggregate (13.88%) affected workability predictions the most. The decrease in workability results from the mixture's increased alkalinity brought on by CaO and the increased aluminosilicate dissolution during the geopolymerization process. This process is linked to the alkaline mixture's lack of water [55]. Fly ash content had the most significant contribution (34.44%) to compressive strength, followed by added water (27.52%). These results concur with an earlier investigation [56] and demonstrate how fly ash content is critical for predicting the compressive strength properties of geopolymers derived from fly ash. Furthermore, the sensitivity analysis of the prediction model demonstrated that the added water strongly influenced the compressive strength prediction. Adding water to the geopolymer concrete increases compressive strength but only to a point, after which additional water reduces compressive strength.

The study aimed to show the benefit of individual and ensemble machine-learning algorithms for calculating the physical and mechanical properties of geopolymers. The MLP, VR, and XGB machine-learning algorithms were used to predict the workability and properties of geopolymers. The XGB model's high accuracy has been previously reported [57,58]. The minimum error values of MAE and MSE for this model further supported this high accuracy. However, evaluating and recommending the best machine-learning regressor for forecasting for a variety of fields is difficult because the model's accuracy is heavily influenced by its parameters and data set. Moreover, ensemble machine-

learning algorithms frequently make use of the weak learner by creating submodels for data training and optimizing for the highest R^2 score. The machine-learning model run for each prediction case may differ depending on the problem's complexity, the prediction's purpose, and the data's characteristics. For instance, [59] demonstrated that the gradient-boosting machine-learning ensemble model achieved the highest accuracy (up to 99%) over the SVC, random forest, and Adaboost models for predicting cardiac disease. The XGBoost ensemble technique nonetheless makes it difficult to demonstrate its advantages, e.g., in the context of stock price prediction, when the quantity of data is limited and the correlation of a single factor is excessively high [60]. Consequently, the prediction results indicate that the multiple linear regression (MLR) single model has the highest accuracy, up to over 90% [61]. Therefore, using ensemble techniques or more intricate models could be beneficial when dealing with large volumes of data or high data complexity, such as imbalanced, fragmentary, or noisy data. In contrast, a simplified machine-learning model can demonstrate greater accuracy when operating with less data, a relatively simple model, or an imbalanced correlation.

Feature importance analysis served to investigate the effect of parameters on the projected workability and compressive strength of geopolymers. Our findings are significant because fly ash is sourced from various locations and coal types that differ in their oxide compounds. By using machine-learning techniques, predictions can be made of the desired properties by determining input parameters. The model parameters and the data set influence the results of the selected models. Our approach can determine those parameters (inputs) having the greatest influence on the predicted output. The associated Python code can also be configured to evaluate or predict any output based on the input parameters.

6. Conclusions

The heterogeneity of fly ash is linked to the varying raw material and its chemical composition, which causes geopolymers to have nonuniform properties. Therefore, creating the optimal geopolymer mix design can be costly and time-consuming. Machine-learning methods can predict the optimal mix design, lowering the cost and time required for geopolymer synthesis. This study used individual machine learning (MLP) and ensemble machine learning (VR and XGB) to predict the workability and compressive strength of fly ash–based geopolymers. The 156 data points from experimental investigations and simulated workability and compressive strength using various models were analyzed. The models were created and trained using ten input parameters. We performed sensitivity analysis on the XGB model to determine the effect of various input features on predictive outcomes. Although all three machine-learning approaches were able to predict geopolymer workability and compressive strength, the XGB model was the most promising, producing the highest R^2 (0.96) and lowest MAE (0.06) and MSE (0.007) for workability, the highest R^2 (0.89), and the lowest MAE (2.45) and MSE (19.57) for compressive strength.

Sensitivity analysis for the XGB model confirmed that the predictions of workability of the fly ash–based geopolymer were affected by the CaO percentage in fly ash (27.13%), followed by added water (14.59%) and fine aggregate (13.88%). Fly ash content was the most important factor in predicting compressive strength, with a sensitivity analysis score of 34.44%, followed by added water (27.52%). This analysis highlights the importance of considering a wide range of input parameters when predicting fly ash–based geopolymer workability and compressive strength and carefully controlling these parameters throughout the manufacturing process. Our results demonstrate that XGB can be used as a reliable machine-learning approach to forecast geopolymer workability and compressive strength. Our approach has practical advantages by reducing the need for extensive testing, lowering labor and material requirements, and providing recommendations for optimizing concrete mix ratios while considering environmental concerns.

Geopolymers can be made from a wide range of industrial by-products. Therefore, future research should focus on prediction modeling that investigates a broader assortment of input and output characteristics. Future geopolymer prediction studies should involve

different raw materials, using comprehensive data sets to assess factors such as freeze–thaw resistance, chloride resistance, sulfate attack, creep, and shrinkage. Furthermore, experimental studies could be conducted to collect additional data and validate the models under different curing conditions.

Author Contributions: A.H. and R.J. contributed to the design of this research project. M.C.K. contributed to MLP, VR, and XGB modeling and critically analyzed and discussed the results of this research. A.H., M.C.K., and R.J. reviewed the initial draft, edited, and prepared the final draft of this manuscript. All authors have read and agreed to the published version of the manuscript.

Funding: This research received no external funding.

Data Availability Statement: The data presented in this study are available on request from the corresponding author.

Acknowledgments: Authors thank the Advanced Materials Processing Laboratory of Institut Teknologi Bandung for the support on this study.

Conflicts of Interest: The authors declare no conflicts of interest.

Appendix A

Fly Ash (g)	CaO (%)	Na_2O (%)	SiO_2 (%)	Fine Aggregate (g)	Molarity	NaOH (g)	WG (g)	Added Water (g)	Curing Temp (°C)	fc (MPa)	Workability (cm)
1260	6.00	1.41	52.30	2268	12	315	315	0	80	62.67	13.50
1260	6.00	1.41	52.30	2268	12	315	315	0	80	62.63	13.50
1260	6.00	1.41	52.30	2268	12	315	315	0	80	62.71	13.50
1260	6.00	1.41	52.30	2268	8	210	420	0	80	54.50	14
1260	6.00	1.41	52.30	2268	8	210	420	0	80	54.48	14
1260	6.00	1.41	52.30	2268	8	210	420	0	80	54.52	14
1260	6.00	1.41	52.30	1890	16	210	420	0	80	80.00	14.50
1260	6.00	1.41	52.30	1890	16	210	420	0	80	79.96	14.50
1260	6.00	1.41	52.30	1890	16	210	420	0	80	80.04	14.50
1260	6.00	1.41	52.30	1890	8	315	315	0	80	59.98	16
1260	6.00	1.41	52.30	1890	8	315	315	0	80	59.96	16
1260	6.00	1.41	52.30	1890	8	315	315	0	80	60.00	16
1260	6.00	1.41	52.30	1890	8	210	420	0	80	53.03	16
1260	6.00	1.41	52.30	1890	8	210	420	0	80	53.02	16
1260	6.00	1.41	52.30	1890	8	210	420	0	80	53.04	16
1260	6.00	1.41	52.30	1512	12	210	420	0	80	61.80	16
1260	6.00	1.41	52.30	1512	12	210	420	0	80	61.76	16
1260	6.00	1.41	52.30	1512	12	210	420	0	80	61.84	16
1260	6.00	1.41	52.30	2268	12	210	420	37.8	80	64.70	16
1260	6.00	1.41	52.30	2268	12	210	420	37.8	80	64.69	16
1260	6.00	1.41	52.30	2268	12	210	420	37.8	80	64.71	16
1260	6.00	1.41	52.30	1890	12	210	420	37.8	80	64.80	16
1260	6.00	1.41	52.30	1890	12	210	420	37.8	80	64.76	16
1260	6.00	1.41	52.30	1890	12	210	420	37.8	80	64.84	16
1260	6.00	1.41	52.30	1890	8	210	420	37.8	80	52.10	17
1260	6.00	1.41	52.30	1890	8	210	420	37.8	80	52.08	17
1260	6.00	1.41	52.30	1890	8	210	420	37.8	80	52.12	17
1260	6.00	1.41	52.30	1890	12	315	315	0	80	73.60	17.50
1260	6.00	1.41	52.30	1890	12	315	315	0	80	73.62	17.50
1260	6.00	1.41	52.30	1890	12	315	315	0	80	73.64	17.50
1260	6.00	1.41	52.30	1890	16	315	315	37.8	80	66.05	18
1260	6.00	1.41	52.30	1890	16	315	315	37.8	80	66.04	18
1260	6.00	1.41	52.30	1890	16	315	315	37.8	80	66.06	18
1260	6.00	1.41	52.30	1890	16	210	420	75.6	80	57.20	18
1260	6.00	1.41	52.30	1890	16	210	420	75.6	80	57.24	18
1260	6.00	1.41	52.30	1890	16	210	420	75.6	80	57.16	18
1260	6.00	1.41	52.30	1890	12	315	315	37.8	80	63.25	18.50
1260	6.00	1.41	52.30	1890	12	315	315	37.8	80	63.30	18.50
1260	6.00	1.41	52.30	1890	12	315	315	37.8	80	63.20	18.50
1260	6.00	1.41	52.30	1890	12	210	420	75.6	80	52.70	18.50
1260	6.00	1.41	52.30	1890	12	210	420	75.6	80	52.80	18.50
1260	6.00	1.41	52.30	1890	12	210	420	75.6	80	52.60	18.50
1260	6.00	1.41	52.30	1890	16	315	315	0	80	63.40	18.50
1260	6.00	1.41	52.30	1890	16	315	315	0	80	63.60	18.50
1260	6.00	1.41	52.30	1890	16	315	315	0	80	63.20	18.50
1260	6.00	1.41	52.30	1890	8	315	315	37.8	80	44.00	19
1260	6.00	1.41	52.30	1890	8	315	315	37.8	80	44.04	19
1260	6.00	1.41	52.30	1890	8	315	315	37.8	80	43.96	19
1260	6.00	1.41	52.30	1512	12	315	315	0	80	63.20	20.50
1260	6.00	1.41	52.30	1512	12	315	315	0	80	63.18	20.50
1260	6.00	1.41	52.30	1512	12	315	315	0	80	63.22	20.50

Fly Ash (g)	CaO (%)	Na_2O (%)	SiO_2 (%)	Fine Aggregate (g)	Molarity	NaOH (g)	WG (g)	Added Water (g)	Curing Temp (°C)	fc (MPa)	Workability (cm)
1260	6.00	1.41	52.30	1512	8	315	315	0	80	55.75	21
1260	6.00	1.41	52.30	1512	8	315	315	0	80	55.90	21
1260	6.00	1.41	52.30	1512	8	315	315	0	80	55.60	21
1260	6.00	1.41	52.30	1890	8	210	420	113.4	80	46.87	21.50
1260	6.00	1.41	52.30	1890	8	210	420	113.4	80	46.86	21.50
1260	6.00	1.41	52.30	1890	8	210	420	113.4	80	46.88	21.50
1260	6.00	1.41	52.30	1890	12	210	420	113.4	80	55.66	22
1260	6.00	1.41	52.30	1890	12	210	420	113.4	80	55.60	22
1260	6.00	1.41	52.30	1890	12	210	420	113.4	80	55.72	22
1260	6.00	1.41	52.30	1890	8	315	315	75.6	80	42.20	22.50
1260	6.00	1.41	52.30	1890	8	315	315	75.6	80	42.10	22.50
1260	6.00	1.41	52.30	1890	8	315	315	75.6	80	42.30	22.50
1260	6.00	1.41	52.30	1890	16	315	315	75.6	80	52.47	22.50
1260	6.00	1.41	52.30	1890	16	315	315	75.6	80	52.48	22.50
1260	6.00	1.41	52.30	1890	16	315	315	75.6	80	52.46	22.50
1260	6.00	1.41	52.30	1890	8	210	420	75.6	80	47.98	23
1260	6.00	1.41	52.30	1890	8	210	420	75.6	80	48.00	23
1260	6.00	1.41	52.30	1890	8	210	420	75.6	80	47.96	23
1260	6.00	1.41	52.30	1890	8	315	315	126	80	33.90	24.50
1260	6.00	1.41	52.30	1890	8	315	315	126	80	33.80	24.50
1260	6.00	1.41	52.30	1890	8	315	315	126	80	34.00	24.50
330	6.00	1.41	52.30	500	8	56.67	113.33	0	25	25.00	24
330	6.00	1.41	52.30	500	8	56.67	113.33	0	25	25.10	24
330	6.00	1.41	52.30	500	8	56.67	113.33	0	25	24.90	24
330	6.00	1.41	52.30	500	12	56.67	113.33	0	25	38.00	21
330	6.00	1.41	52.30	500	12	56.67	113.33	0	25	38.04	21
330	6.00	1.41	52.30	500	12	56.67	113.33	0	25	37.96	21
330	6.00	1.41	52.30	500	16	56.67	113.33	0	25	32.00	16
330	6.00	1.41	52.30	500	16	56.67	113.33	0	25	31.98	16
330	6.00	1.41	52.30	500	16	56.67	113.33	0	25	32.02	16
330	6.00	1.41	52.30	500	8	56.67	113.33	0	80	26.00	24
330	6.00	1.41	52.30	500	8	56.67	113.33	0	80	26.01	24
330	6.00	1.41	52.30	500	8	56.67	113.33	0	80	25.99	24
330	6.00	1.41	52.30	500	12	56.67	113.33	0	80	52.00	21
330	6.00	1.41	52.30	500	12	56.67	113.33	0	80	52.02	21
330	6.00	1.41	52.30	500	12	56.67	113.33	0	80	51.98	21
330	6.00	1.41	52.30	500	16	56.67	113.33	0	80	45.00	16
330	6.00	1.41	52.30	500	16	56.67	113.33	0	80	45.20	16
330	6.00	1.41	52.30	500	16	56.67	113.33	0	80	44.80	16
330	6.00	1.41	52.30	500	12	56.67	113.33	0	10	45.00	24
330	6.00	1.41	52.30	500	12	56.67	113.33	0	10	45.10	24
330	6.00	1.41	52.30	500	12	56.67	113.33	0	10	44.90	24
630	15.85	0.93	40.18	945	16	105	210	0	80	41.97	10
630	15.85	0.93	40.18	945	16	105	210	0	80	41.96	10
630	15.85	0.93	40.18	945	16	105	210	0	80	41.98	10
630	15.85	0.93	40.18	756	12	105	210	0	80	41.17	9
630	15.85	0.93	40.18	756	12	105	210	0	80	41.16	9
630	15.85	0.93	40.18	756	12	105	210	0	80	41.18	9
630	15.85	0.93	40.18	1134	8	105	210	0	80	36.72	10
630	15.85	0.93	40.18	1134	8	105	210	0	80	36.72	10
630	15.85	0.93	40.18	1134	8	105	210	0	80	36.72	10
630	15.85	0.93	40.18	945	12	157.5	157.5	0	80	25.90	10
630	15.85	0.93	40.18	945	12	157.5	157.5	0	80	25.80	10
630	15.85	0.93	40.18	945	12	157.5	157.5	0	80	26.00	10
630	15.85	0.93	40.18	1134	12	157.5	157.5	0	80	32.32	10
630	15.85	0.93	40.18	1134	12	157.5	157.5	0	80	32.36	10
630	15.85	0.93	40.18	1134	12	157.5	157.5	0	80	32.28	10
630	15.85	0.93	40.18	756	8	157.5	157.5	0	80	44.73	10
630	15.85	0.93	40.18	756	8	157.5	157.5	0	80	44.72	10
630	15.85	0.93	40.18	756	8	157.5	157.5	0	80	44.74	10
630	15.85	0.93	40.18	945	16	157.5	157.5	0	80	42.40	10
630	15.85	0.93	40.18	945	16	157.5	157.5	0	80	42.36	10
630	15.85	0.93	40.18	945	16	157.5	157.5	0	80	42.44	10
630	15.85	0.93	40.18	945	12	157.5	157.5	18.9	80	46.20	10
630	15.85	0.93	40.18	945	12	157.5	157.5	18.9	80	46.10	10
630	15.85	0.93	40.18	945	12	157.5	157.5	18.9	80	46.30	10
630	15.85	0.93	40.18	945	8	157.5	157.5	18.9	80	61.45	10
630	15.85	0.93	40.18	945	8	157.5	157.5	18.9	80	61.46	10
630	15.85	0.93	40.18	945	8	157.5	157.5	18.9	80	61.44	10
630	15.85	0.93	40.18	945	16	157.5	157.5	37.8	80	21.72	10
630	15.85	0.93	40.18	945	16	157.5	157.5	37.8	80	21.76	10
630	15.85	0.93	40.18	945	16	157.5	157.5	37.8	80	21.68	10
630	15.85	0.93	40.18	945	8	157.5	157.5	37.8	80	30.51	12
630	15.85	0.93	40.18	945	8	157.5	157.5	37.8	80	30.50	12
630	15.85	0.93	40.18	945	8	157.5	157.5	37.8	80	30.52	12
630	15.85	0.93	40.18	945	8	157.5	157.5	63	80	44.67	10.50
630	15.85	0.93	40.18	945	8	157.5	157.5	63	80	44.68	10.50
630	15.85	0.93	40.18	945	8	157.5	157.5	63	80	44.66	10.50
630	15.85	0.93	40.18	945	16	157.5	157.5	18.9	80	35.72	11.50
630	15.85	0.93	40.18	945	16	157.5	157.5	18.9	80	35.76	11.50
630	15.85	0.93	40.18	945	16	157.5	157.5	18.9	80	35.68	11.50

Fly Ash (g)	CaO (%)	Na_2O (%)	SiO_2 (%)	Fine Aggregate (g)	Molarity	NaOH (g)	WG (g)	Added Water (g)	Curing Temp (°C)	fc (MPa)	Workability (cm)
630	15.85	0.93	40.18	945	8	105	210	0	80	50.33	12
630	15.85	0.93	40.18	945	8	105	210	0	80	50.32	12
630	15.85	0.93	40.18	945	8	105	210	0	80	50.34	12
630	15.85	0.93	40.18	945	12	105	210	0	80	47.50	11
630	15.85	0.93	40.18	945	12	105	210	0	80	47.52	11
630	15.85	0.93	40.18	945	12	105	210	0	80	47.48	11
630	15.85	0.93	40.18	945	12	157.5	157.5	63	80	53.90	13
630	15.85	0.93	40.18	945	12	157.5	157.5	63	80	53.80	13
630	15.85	0.93	40.18	945	12	157.5	157.5	63	80	54.00	13
630	15.85	0.93	40.18	945	16	157.5	157.5	63	80	30.38	12
630	15.85	0.93	40.18	945	16	157.5	157.5	63	80	30.36	12
630	15.85	0.93	40.18	945	16	157.5	157.5	63	80	30.40	12
630	15.85	0.93	40.18	756	8	105	210	0	80	32.12	13.50
630	15.85	0.93	40.18	756	8	105	210	0	80	32.08	13.50
630	15.85	0.93	40.18	756	8	105	210	0	80	32.16	13.50
630	15.85	0.93	40.18	756	16	105	210	0	80	33.15	13.50
630	15.85	0.93	40.18	756	16	105	210	0	80	33.16	13.50
630	15.85	0.93	40.18	756	16	105	210	0	80	33.14	13.50
630	15.85	0.93	40.18	1134	12	105	210	0	80	42.15	15
630	15.85	0.93	40.18	1134	12	105	210	0	80	42.10	15
630	15.85	0.93	40.18	1134	12	105	210	0	80	42.20	15
630	15.85	0.93	40.18	1134	16	105	210	0	80	41.73	13
630	15.85	0.93	40.18	1134	16	105	210	0	80	41.74	13
630	15.85	0.93	40.18	1134	16	105	210	0	80	41.72	13

References

1. Ansari, M.A.; Shariq, M.; Mahdi, F. Geopolymer concrete for clean and sustainable construction—A state-of-the-art review on the mix design approaches. *Structures* **2023**, *55*, 1045–1070. [CrossRef]
2. Jamieson, E.; McLellan, B.; van Riessen, A.; Nikraz, H. Comparison of embodied energies of Ordinary Portland Cement with Bayer-derived geopolymer products. *J. Clean. Prod.* **2015**, *99*, 112–118. [CrossRef]
3. Cong, P.; Cheng, Y. Advances in geopolymer materials: A comprehensive review. *J. Traffic Transp. Eng. (Engl. Ed.)* **2021**, *8*, 283–314. [CrossRef]
4. Alterary, S.S.; Marei, N.H. Fly ash properties, characterization, and applications: A review. *J. King Saud. Univ. Sci.* **2021**, *33*, 101536. [CrossRef]
5. Bhatt, A.; Priyadarshini, S.; Acharath Mohanakrishnan, A.; Abri, A.; Sattler, M.; Techapaphawit, S. Physical, chemical, and geotechnical properties of coal fly ash: A global review. *Case Stud. Constr. Mater.* **2019**, *11*, e00263. [CrossRef]
6. *ASTM C618*; Standard Specification for Coal Fly Ash and Raw or Calcined Natural Pozzolan for Use in Concrete. ASTM International: West Conshohocken, PA, USA, 2022.
7. Turan, C.; Javadi, A.A.; Vinai, R. Effects of Class C and Class F Fly Ash on Mechanical and Microstructural Behavior of Clay Soil-A Comparative Study. *Materals* **2022**, *15*, 1845. [CrossRef] [PubMed]
8. Wang, Q.; Ahmad, W.; Ahmad, A.; Aslam, F.; Mohamed, A.; Vatin, N.I. Application of Soft Computing Techniques to Predict the Strength of Geopolymer Composites. *Polymers* **2022**, *14*, 1074. [CrossRef] [PubMed]
9. Nazar, S.; Yang, J.; Amin, M.N.; Khan, K.; Ashraf, M.; Aslam, F.; Javed, M.F.; Eldin, S.M. Machine learning interpretable-prediction models to evaluate the slump and strength of fly ash-based geopolymer. *J. Mater. Res. Technol.* **2023**, *24*, 100–124. [CrossRef]
10. Shah, S.F.A.; Chen, B.; Zahid, M.; Ahmad, M.R. Compressive strength prediction of one-part alkali activated material enabled by interpretable machine learning. *Constr. Build. Mater.* **2022**, *360*, 129534. [CrossRef]
11. Amin, M.N.; Khan, K.; Javed, M.F.; Aslam, F.; Qadir, M.G.; Faraz, M.I. Prediction of Mechanical Properties of Fly-Ash/Slag-Based Geopolymer Concrete Using Ensemble and Non-Ensemble Machine-Learning Techniques. *Materials* **2022**, *15*, 3478. [CrossRef]
12. Huang, B.; Bahrami, A.; Javed, M.F.; Azim, I.; Iqbal, M.A. Evolutionary Algorithms for Strength Prediction of Geopolymer Concrete. *Buildings* **2024**, *14*, 1347. [CrossRef]
13. Harmaji, A.; Sunendar, B. Utilization of Fly Ash, Red Mud, and Electric Arc Furnace Dust Slag for Geopolymer. *Mater. Sci. Forum* **2016**, *841*, 157–161. [CrossRef]
14. *ASTM C1437*; Standard Test Method for Flow of Hydraulic Cement Mortar. ASTM International: West Conshohocken, PA, USA, 2020.
15. *ASTM C39*; Standard Test Method for Compressive Strength of Cylindrical Concrete Specimens. ASTM International: West Conshohocken, PA, USA, 2021.
16. Kilimci, Z.H. Ensemble Regression-Based Gold Price (XAU/USD) Prediction. *J. Emerg. Comput. Technol.* **2022**, *2*, 7–12.
17. Mohammed, A.; Kora, R. A comprehensive review on ensemble deep learning: Opportunities and challenges. *J. King Saud. Univ. Comput. Inf. Sci.* **2023**, *35*, 757–774. [CrossRef]
18. Chen, T.; Guestrin, C. XGBoost: A Scalable Tree Boosting System. In Proceedings of the 22nd ACM SIGKDD International Conference on Knowledge Discovery and Data Mining, San Francisco, CA, USA, 13–17 August 2016; pp. 785–794.
19. Li, Z.; Lu, T.; He, X.; Montillet, J.-P.; Tao, R. An improved cyclic multi model-eXtreme gradient boosting (CMM-XGBoost) forecasting algorithm on the GNSS vertical time series. *Adv. Space Res.* **2023**, *71*, 912–935. [CrossRef]
20. Chakraborty, D.; Awolusi, I.; Gutierrez, L. An explainable machine learning model to predict and elucidate the compressive behavior of high-performance concrete. *Results Eng.* **2021**, *11*, 100245. [CrossRef]

21. Chandra, R. *Parallel Programming in OpenMP*; Morgan Kaufmann: Burlington, MA, USA, 2001.
22. Shang, M.; Li, H.; Ahmad, A.; Ahmad, W.; Ostrowski, K.A.; Aslam, F.; Joyklad, P.; Majka, T.M. Predicting the mechanical properties of RCA-based concrete using supervised machine learning algorithms. *Materials* **2022**, *15*, 647. [CrossRef]
23. Song, H.; Ahmad, A.; Ostrowski, K.A.; Dudek, M. Analyzing the compressive strength of ceramic waste-based concrete using experiment and artificial neural network (ANN) approach. *Materials* **2021**, *14*, 4518. [CrossRef]
24. Simatupang, P.H.; Imran, I.; Pane, I.; Sunendar, B. On the Development of a Nomogram for Alkali Activated Fly Ash Material (AAFAM) Mixtures. *J. Eng. Technol. Sci.* **2015**, *47*, 231–249. [CrossRef]
25. Aliabdo, A.A.; Abd Elmoaty, A.E.M.; Salem, H.A. Effect of water addition, plasticizer and alkaline solution constitution on fly ash based geopolymer concrete performance. *Constr. Build. Mater.* **2016**, *121*, 694–703. [CrossRef]
26. Waqas, R.M.; Butt, F.; Zhu, X.; Jiang, T.; Tufail, R.F. A Comprehensive Study on the Factors Affecting the Workability and Mechanical Properties of Ambient Cured Fly Ash and Slag Based Geopolymer Concrete. *Appl. Sci.* **2021**, *11*, 8722. [CrossRef]
27. Sasui, S.; Kim, G.; Nam, J.; Koyama, T.; Chansomsak, S. Strength and Microstructure of Class-C Fly Ash and GGBS Blend Geopolymer Activated in NaOH & NaOH + Na(2)SiO(3). *Materials* **2019**, *13*, 59. [CrossRef] [PubMed]
28. Chen, Y.; de Lima, L.M.; Li, Z.; Ma, B.; Lothenbach, B.; Yin, S.; Yu, Q.; Ye, G. Synthesis, solubility and thermodynamic properties of N-A-S-H gels with various target Si/Al ratios. *Cem. Concr. Res.* **2024**, *180*, 107484. [CrossRef]
29. Li, Z.; Zhang, J.; Wang, M. Structure, Reactivity, and Mechanical Properties of Sustainable Geopolymer Material: A Reactive Molecular Dynamics Study. *Front. Mater.* **2020**, *7*. [CrossRef]
30. Castillo, H.; Collado, H.; Droguett, T.; Sánchez, S.; Vesely, M.; Garrido, P.; Palma, S. Factors Affecting the Compressive Strength of Geopolymers: A Review. *Minerals* **2021**, *11*, 1317. [CrossRef]
31. Bernal, S. The resistance of alkali-activated cement-based binders to carbonation. In *Handbook of Alkali-Activated Cements, Mortars and Concretes*; Elsevier: Sawston, UK, 2015; pp. 319–332.
32. Morandeau, A.; Thiery, M.; Dangla, P. Investigation of the carbonation mechanism of CH and CSH in terms of kinetics, microstructure changes and moisture properties. *Cem. Concr. Res.* **2014**, *56*, 153–170. [CrossRef]
33. Ye, H.; Cai, R.; Tian, Z. Natural carbonation-induced phase and molecular evolution of alkali-activated slag: Effect of activator composition and curing temperature. *Constr. Build. Mater.* **2020**, *248*, 118726. [CrossRef]
34. Kozhukhova, N.; Kozhukhova, M.; Zhernovskaya, I.; Promakhov, V. The Correlation of Temperature-Mineral Phase Transformation as a Controlling Factor of Thermal and Mechanical Performance of Fly Ash-Based Alkali-Activated Binders. *Materials* **2020**, *13*, 5181. [CrossRef]
35. Djobo, J.N.Y.; Elimbi, A.; Tchakouté, H.K.; Kumar, S. Reactivity of volcanic ash in alkaline medium, microstructural and strength characteristics of resulting geopolymers under different synthesis conditions. *J. Mater. Sci.* **2016**, *51*, 10301–10317. [CrossRef]
36. Tchadjié, L.N.; Djobo, J.N.Y.; Ranjbar, N.; Tchakouté, H.K.; Kenne, B.B.D.; Elimbi, A.; Njopwouo, D. Potential of using granite waste as raw material for geopolymer synthesis. *Ceram. Int.* **2016**, *42*, 3046–3055. [CrossRef]
37. Onutai, S.; Osugi, T.; Sone, T. Alumino-Silicate Structural Formation during Alkali-Activation of Metakaolin: In-Situ and Ex-Situ ATR-FTIR Studies. *Materials* **2023**, *16*, 985. [CrossRef] [PubMed]
38. Luo, X.; Huang, L.; Li, Y.; Chen, Z. Preparation of geopolymers from thermally activated lithium slag as sole precursor: Mechanical properties and microstructure. *Case Stud. Constr. Mater.* **2024**, *20*, e03248. [CrossRef]
39. Chen, L.; Wang, Z.; Wang, Y.; Feng, J. Preparation and Properties of Alkali Activated Metakaolin-Based Geopolymer. *Materials* **2016**, *9*, 767. [CrossRef] [PubMed]
40. Król, M.; Koleżyński, A.; Mozgawa, W. Vibrational Spectra of Zeolite Y as a Function of Ion Exchange. *Molecules* **2021**, *26*, 342. [CrossRef]
41. Ritz, M. Infrared and Raman Spectroscopy of Mullite Ceramics Synthesized from Fly Ash and Kaolin. *Minerals* **2023**, *13*, 864. [CrossRef]
42. Mishra, J.; Nanda, B.; Patro, S.K.; Krishna, R.S. Sustainable Fly Ash Based Geopolymer Binders: A Review on Compressive Strength and Microstructure Properties. *Sustainability* **2022**, *14*, 15062. [CrossRef]
43. Yazid, M.H.; Faris, M.A.; Abdullah, M.; Ibrahim, M.S.I.; Razak, R.A.; Burduhos Nergis, D.D.; Burduhos Nergis, D.P.; Benjeddou, O.; Nguyen, K.S. Mechanical Properties of Fly Ash-Based Geopolymer Concrete Incorporation Nylon66 Fiber. *Materials* **2022**, *15*, 9050. [CrossRef]
44. Beltrame, N.A.M.; Dias, R.L.; Witzke, F.B.; Medeiros-Junior, R.A. Effect of carbonation curing on the physical, mechanical, and microstructural properties of metakaolin-based geopolymer concrete. *Constr. Build. Mater.* **2023**, *406*, 133403. [CrossRef]
45. Sun, Z.; Vollpracht, A. One year geopolymerisation of sodium silicate activated fly ash and metakaolin geopolymers. *Cem. Concr. Compos.* **2019**, *95*, 98–110. [CrossRef]
46. Longhi, M.A.; Rodríguez, E.D.; Walkley, B.; Zhang, Z.; Kirchheim, A.P. Metakaolin-based geopolymers: Relation between formulation, physicochemical properties and efflorescence formation. *Compos. Part B Eng.* **2020**, *182*, 107671. [CrossRef]
47. Zhang, J.; Shi, C.; Zhang, Z. Carbonation induced phase evolution in alkali-activated slag/fly ash cements: The effect of silicate modulus of activators. *Constr. Build. Mater.* **2019**, *223*, 566–582. [CrossRef]
48. Zhao, C.; Li, Z.; Peng, S.; Liu, J.; Wu, Q.; Xu, X. State-of-the-art review of geopolymer concrete carbonation: From impact analysis to model establishment. *Case Stud. Constr. Mater.* **2024**, *20*, e03124. [CrossRef]
49. Ollivier, J.P.; Maso, J.C.; Bourdette, B. Interfacial transition zone in concrete. *Adv. Cem. Based Mater.* **1995**, *2*, 30–38. [CrossRef]

50. Alanazi, H. Study of the Interfacial Transition Zone Characteristics of Geopolymer and Conventional Concretes. *Gels* **2022**, *8*, 105. [CrossRef]
51. Luo, Z.; Li, W.; Wang, K.; Castel, A.; Shah, S.P. Comparison on the properties of ITZs in fly ash-based geopolymer and Portland cement concretes with equivalent flowability. *Cem. Concr. Res.* **2021**, *143*, 106392. [CrossRef]
52. Pelalak, R.; Nakhjiri, A.T.; Marjani, A.; Rezakazemi, M.; Shirazian, S. Influence of machine learning membership functions and degree of membership function on each input parameter for simulation of reactors. *Sci. Rep.* **2021**, *11*, 1891. [CrossRef]
53. Ahmad, A.; Ostrowski, K.A.; Maślak, M.; Farooq, F.; Mehmood, I.; Nafees, A. Comparative study of supervised machine learning algorithms for predicting the compressive strength of concrete at high temperature. *Materials* **2021**, *14*, 4222. [CrossRef]
54. Naderpour, H.; Rafiean, A.H.; Fakharian, P. Compressive strength prediction of environmentally friendly concrete using artificial neural networks. *J. Build. Eng.* **2018**, *16*, 213–219. [CrossRef]
55. Rashad, A.M.; Gharieb, M. Solving the perpetual problem of imperative use heat curing for fly ash geopolymer cement by using sugar beet waste. *Constr. Build. Mater.* **2021**, *307*, 124902. [CrossRef]
56. Ahmad, A.; Ahmad, W.; Chaiyasarn, K.; Ostrowski, K.A.; Aslam, F.; Zajdel, P.; Joyklad, P. Prediction of Geopolymer Concrete Compressive Strength Using Novel Machine Learning Algorithms. *Polymers* **2021**, *13*, 3389. [CrossRef]
57. Safhi, A.e.M.; Dabiri, H.; Soliman, A.; Khayat, K.H. Prediction of self-consolidating concrete properties using XGBoost machine learning algorithm: Part 1—Workability. *Constr. Build. Mater.* **2023**, *408*, 133560. [CrossRef]
58. Ahmed, A.; Song, W.; Zhang, Y.; Haque, M.A.; Liu, X. Hybrid BO-XGBoost and BO-RF Models for the Strength Prediction of Self-Compacting Mortars with Parametric Analysis. *Materials* **2023**, *16*, 4366. [CrossRef] [PubMed]
59. Kumar, K.J.; Thanka, M.R.; Edwin, E.B.; Ebenezer, V.; Joy, P. Multi-Model Supervised Machine Learning Techniques for Heart Stroke Prediction. In Proceedings of the 2024 International Conference on Expert Clouds and Applications (ICOECA), Bengaluru, India, 18–19 April 2024; pp. 661–665.
60. Deng, S.; Huang, X.; Zhu, Y.; Su, Z.; Fu, Z.; Shimada, T. Stock index direction forecasting using an explainable eXtreme Gradient Boosting and investor sentiments. *N. Am. J. Econ. Financ.* **2023**, *64*, 101848. [CrossRef]
61. Shao, G. Stock price prediction based on multifactorial linear models and machine learning approaches. In Proceedings of the 2022 IEEE Conference on Telecommunications, Optics and Computer Science (TOCS), Dalian, China, 11–12 December 2022; pp. 319–324.

Disclaimer/Publisher's Note: The statements, opinions and data contained in all publications are solely those of the individual author(s) and contributor(s) and not of MDPI and/or the editor(s). MDPI and/or the editor(s) disclaim responsibility for any injury to people or property resulting from any ideas, methods, instructions or products referred to in the content.